View metadata, citation and similar papers at core.ac.uk

brought to you by CORE

provided by Queen Mary Research Online

NOTICE: this is the author's version of a work that was accepted for publication in ***Solid State Ionics***. Changes resulting from the publishing process, such as peer review, editing, corrections, structural formatting, and other quality control mechanisms may not be reflected in this document. Changes may have been made to this work since it was submitted for publication. A definitive version was subsequently published in **Solid State Ionics 269 (2015) 37; doi: 10.1016/j.ssi.2014.11.012**

The double rare-earth substituted bismuth oxide system $Bi_3Y_{1-x}Yb_xO_6$

M. Leszczynska,[a] A. Borowska-Centkowska,[a] M. Malys,[a] J.R. Dygas,[a] F. Krok,[a] W. Wrobel[a*] and I. Abrahams[b*]

[a]Faculty of Physics, Warsaw University of Technology, ul. Koszykowa 75, 00-662 Warszawa, Poland.

[b]Materials Research Institute, Department of Chemistry and Biochemistry, School of Biological and Chemical Sciences, Queen Mary University of London, Mile End Road, London E1 4NS, U.K.

*Corresponding authors: I. Abrahams e –mail: i.abrahams@qmul.ac.uk
W. Wrobel e–mail: wrobel@if.pw.edu.pl

Abstract

Structure and electrical conductivity in the double rare-earth substituted system $Bi_3Y_{1-x}Yb_xO_6$ ($0.00 \leq x \leq 1.00$) is discussed. Structural characterisation, by X-ray and neutron powder diffraction, confirms a full δ-Bi_2O_3 type solid solution. This structure is maintained up to 850°C, with no visible evidence for phase separation over the timescale of the diffraction experiments. Small compositional changes in oxide ion distribution are observed, with Yb rich compositions favouring a more centralised oxide ion distribution in the tetrahedral cavities. Electrical characterisation, by a.c. impedance spectroscopy, reveals the system to be highly conducting, with measurements of transference number indicating this conductivity to be almost purely ionic at temperatures above *ca*. 600°C. At lower temperatures, transference number decreases with increasing ytterbium content. Maxima in activation energy and conductivity pre-exponential factor at high temperatures are observed at $x = 0.50$ and are discussed in terms of changes in configurational entropy. This behaviour resembles the "mixed alkali effect" frequently observed in glasses. However, in the present case there is no corresponding minimum in conductivity and the effect is associated with the immobile sublattice.

Keywords: Bismuth oxide; bismuth yttrium ytterbium oxide; fluorite structure; neutron diffraction; X-ray diffraction; a.c. impedance spectroscopy; transference number.

1. Introduction

Despite their relative instability under reducing conditions, bismuth oxide based electrolytes have attracted a great deal of attention, due to their exceptionally high oxide ion conductivities at relatively low temperatures. Recently, it has been shown that through careful design of the electrolyte and device construction, these materials can be utilised in intermediate temperature solid oxide fuel cells (IT-SOFCs) [1,2]. The δ-phase of Bi_2O_3 exhibits the highest known oxide ion conductivity of any solid and represents the benchmark for oxide ion conducting solid electrolytes. Unfortunately, this high temperature polymorph is stable only at elevated temperatures (above *ca*. 730°C [3]) and readily transforms to more poorly conducting phases (α, β and γ) at lower temperatures, depending on cooling conditions. Stabilisation of the δ-phase to room temperature, can be achieved by solid solution formation with other metal oxides, in particular the rare-earth oxides RE_2O_3 [4-9]. It has been argued that many of these so called "stabilised" phases are in fact metastable and that annealing at intermediate temperatures, around 600°C, invariably leads to the formation of stable phases or phase separation [10,11]. However, double substitution has been acknowledged as a route to truly stable δ-type phases [12-15]. In these systems, it has been argued that the increased stability arises from increased configurational entropy [16,17].

Both the systems Bi_2O_3-Y_2O_3 [3,10,11,18-21] and Bi_2O_3-Yb_2O_3 [20,22-27] yield face centred cubic (fcc) fluorite phases over wide compositional ranges. The widely studied Bi_2O_3-Y_2O_3 system shows exceptionally high conductivity and is reviewed elsewhere [7]. At 25% Y_2O_3 substitution, the fcc phase is readily obtained at room temperature and its structure has been confirmed as a fully disordered δ-Bi_2O_3 type phase [28,29].

Despite early claims that the fcc phase could not be stabilised in the Bi_2O_3-Yb_2O_3 system [20], it was later found that this phase could indeed be obtained, depending on composition and thermal treatment [22]. In the most recent study of the Bi_2O_3-Yb_2O_3 equilibrium phase diagram [24], the fcc phase is reported to be stable at higher temperatures, in compositions around 25% substitution of Bi by Yb, with phase separation occurring at lower temperatures. Of the rare earth substituted bismuth oxides, the Yb substituted system shows the highest conductivity decay on prolonged annealing at 500°C [25-27]. This has been associated with a redistribution of the oxide ions as well as vacancy ordering.

In the present study, structure and conductivity in the double rare-earth substituted pseudo-binary system Bi_3YO_6-Bi_3YbO_6 is investigated. Y^{3+} and Yb^{3+} have similar ionic radii (0.900 Å and 0.868 Å, for six-coordinate geometry with oxide ions [30]) and being isovalent

with Bi^{3+}, this system allows for a study of the effects of double substitution in isolation from changes in nominal vacancy concentration and long-range ordering.

2. Experimental

2.1 Preparations

Samples of general composition $Bi_3Y_{1-x}Yb_xO_6$ ($0.00 \leq x \leq 1.00$) were prepared using stoichiometric amounts of Bi_2O_3 (Sigma Aldrich, 99.9%), Y_2O_3 (Sigma Aldrich, 99.99%) and Yb_2O_3 (Sigma Aldrich, 99.9%). The starting mixtures were ground in ethanol using a planetary ball mill with agate balls in an agate cup for 24 h at 400 rpm. The dried mixtures were heated at 750°C for 24 h, then cooled and reground. The samples were then reheated at 950°C for a further 24 h, before cooling in air to room temperature, over a period of approximately 5 h. For electrical measurements, synthesised powders were pelletised, pressed isostatically at a pressure of 400 MPa and sintered at 950°C for 10 h, before cooling in air to room temperature over a period of *ca*. 5 h.

2.2 Electrical measurements

Electrical parameters were determined by a.c. impedance spectroscopy up to *ca*. 840°C, using a fully automated Solartron 1255/1286 system, in the frequency range 1 Hz to 5×10^5 Hz, with a signal strength of 50 mV. Samples for impedance measurements were prepared as rectangular blocks (*ca.* $6 \times 3 \times 3$ mm^3) cut from sintered pellets, using a diamond saw. Platinum electrodes were sputtered by cathodic discharge on the two smallest faces. Impedance spectra were acquired over two cycles of heating and cooling at stabilised temperatures. Impedance at each frequency was measured repeatedly until consistency (2% tolerance in drift) was achieved or a maximum number of 25 repeats had been reached, using an algorithm described earlier [31]. We have previously reported electrical parameters for the $x = 0.00$ composition [29]. These have been re-measured in the present study over a greater temperature range.

For the $x = 0.00$, 0.50 and 1.00 compositions, the ionic and electronic contributions to the total conductivity were measured using a modified EMF method, with an external adjustable voltage source in the concentration cell $O_2(pO_2 = 1.01 \times 10^5$ Pa): Pt | oxide | Pt : O_2 ($pO_2 = 0.2095 \times 10^5$ Pa), as described in detail elsewhere [32]. Measurements were performed on cooling between *ca*. 820°C and *ca*. 450°C at stabilised temperatures.

2.3 Diffraction

X-ray powder diffraction data were obtained on a Philips X'Pert Pro diffractometer fitted with an X'Celerator detector, using Ni filtered Cu-Kα radiation (λ_1 = 1.54056 Å and λ_2 = 1.54439 Å). Data were collected in flat plate θ/θ geometry and calibrated against an external Si standard. Room temperature data, suitable for detailed Rietveld refinement, were collected in the 2θ range 5-125°, in steps of 0.0167°, with an effective scan time of 250 s per step. Elevated temperature measurements were made using an Anton Paar HTK-1200 camera. Samples were mounted on a Pt coated ceramic sample holder and data collected in steps of 50°C from 100°C to 850°C, in the 2θ range 5-125°, with a step width of 0.033° and an effective scan time of 50 s per step.

Neutron powder diffraction data were obtained on the Polaris diffractometer at the ISIS Facility, Rutherford Appleton Laboratory at room temperature. Data collected on the back-scattering (130-160°), and low-angle (28-42°) detectors were used in subsequent refinements. Samples were contained in cylindrical vanadium cans of 11 mm diameter, located in front of the back-scattering detectors. Data were collected for *ca*. 200 μA h for each sample.

Structure refinement was carried out by Rietveld analysis using the GSAS suite of programs [33]. For the room temperature structures, combined refinements using X-ray and neutron data were carried out. A cubic model in space group *Fm*-3*m* was used for all refinements, with Bi, Y and Yb located on the ideal 4*a* site (0,0,0) [34]. O atoms were refined on three crystallographically distinct sites 8*c*, 32*f* and 48*i*. Isotropic thermal parameters for the oxygen atoms were tied to a single value and a total oxide occupancy constraint applied. Crystal and refinement parameters for the room temperature analyses are summarised in Table 1, with the fitted diffraction profiles given in Fig. 1. For elevated temperatures, where only X-ray data were available, the oxygen atom coordinates were not refined.

2.4 Thermal Analysis

Differential thermal analysis (DTA) was carried out using a TA Instruments Q600 scanning differential thermal analyser. Approximately 60 mg of powdered sample in an alumina

crucible was monitored over heating and cooling cycles, between ambient temperature and 1000°C, at a heating rate of 20°C min^{-1} in flowing air.

3. Results and discussion

As seen in Fig. 1, all peaks in the diffraction patterns at room temperature can be indexed on a cubic *Fm*-3*m* cell, with no evidence for superlattice ordering or phase separation. The compositional variation of the cubic lattice parameter at room temperature and at 800°C is shown in Fig. 2. Despite the small difference in ionic radius for Y^{3+} and Yb^{3+} cations, a general decrease in cubic lattice parameter with increasing Yb content is observed. There is a small increase in lattice parameter between x = 0.75 and x =1.00, although it should be noted that this apparent increase may be due to small differences in the instrument calibration, as the data for x =1.00 were collected earlier as part of another study [35]. The plots appear to confirm full disorder of the dopant cations, with no evidence of clustering (such as the appearance of a miscibility dome).

Variable temperature X-ray results confirm that the fluorite structure is maintained up to 850°C in all the studied compositions. Fig. 3 shows the thermal variation of the X-ray diffraction pattern for the x = 0.50 composition, which is typical. Again no evidence is seen for phase separation, a problem that is known to occur in ytterbium substituted bismuth oxide [24,36]. The thermal variation of cubic lattice parameter for the studied compositions is shown in Fig. 4. The plots can be described as being divided into two approximately linear regions, one at higher temperatures and another at lower temperatures, with a transition between the two regions at around 400 to 500°C. This type of transition has previously been associated with changes in the oxide ion/vacancy distribution in the two end member compositions Bi_3YO_6 [29] and Bi_3YbO_6 [35].

The DTA thermograms for the studied compositions showed no major thermal features up to 1000°C that would account for the change in the thermal expansion of the cubic lattice parameter at intermediate temperatures. That for the x = 0.50 composition is representative and is shown in Fig. 5.

Table 2 shows the refined structural parameters and significant contact distances for the studied compositions at room temperature. Oxide ions are distributed over three crystallographically distinct sites. O1 corresponds to the ideal fluorite 8*c* site, while O2 (32*f*) is a position close to the 8*c* site, but shifted in the <111> direction towards the corner of the tetrahedral cavity of the fcc lattice. O3 is located in an interstitial site (48*i*), which is only

found to be occupied in substituted bismuth oxides and is associated with the dopant cation coordination environment [29,34,36]. The compositional variation of the oxide ion site occupancies is shown in Fig. 6. There is a small increase in the 48*i* site occupancy with increasing *x*-value above $x = 0.50$. This increase is at the expense of ions in the tetrahedral cavity. The most significant change is the increase in 32*f* site occupancy at the expense of that of the 8*c* site, with increasing level of ytterbium content. It should be noted here, that since both these sites reside within the tetrahedral cavity of the fcc lattice, their site occupancies are highly correlated with each other and that the relative occupancies of these two sites reflects the degree of positional/thermal disorder of the oxide ions in the tetrahedral cavity. Oxide ions in the 48*i* site may be considered as Frenkel interstitials, *i.e.*

$$O_x \rightarrow V_O^{\bullet\bullet} + O_i^{''} \qquad (1)$$

As a result, the vacancy concentration in the tetrahedral cavity increases with respect to the nominal vacancy concentration of two vacancies per cell [29,36].

Arrhenius plots of total electrical conductivity are shown in Fig. 7. For compositions $x \leq 0.50$, plots are fully reproducible on heating and cooling and essentially show two approximately linear regions, with different activation energies and transitions between these two regions in the range *ca*. 500°C to 650°C. For the Yb rich compositions, some thermal hysteresis is observed at intermediate temperatures (*ca*. 500 to 650 °C for $x = 0.75$ and *ca*. 550 to 700°C for $x = 1.00$). Fig. 8 shows the Arrhenius plots for the $x = 1.00$ composition after successive heating and cooling runs. The thermal hysteresis is clearly visible at intermediate temperatures, with a knee shaped feature in the transitional region. This feature is much less pronounced in the $x = 0.75$ composition. We have previously attributed this type of feature in a more bismuth rich ytterbate composition, $Bi_4YbO_{7.5}$, to the onset of phase separation at intermediate temperatures [36]. In the case of Bi_3YbO_6, no evidence of phase separation was seen in the X-ray and neutron diffraction patterns at these temperatures [35]. Similarly, the X-ray data for the $x = 0.75$ composition showed no evidence of phase separation. It is likely that the hysteresis seen in the $x = 1.00$ and $x = 0.75$ compositions is analogous to that seen in $Bi_4YbO_{7.5}$, but that the kinetics of the phase separation are significantly slower in these more heavily substituted compositions. These results appear to confirm the metastability of the δ-phase at temperatures below *ca*. 600°C in this system and

are consistent with the high conductivity decay at intermediate temperatures [25-29] and the Bi_2O_3-Yb_2O_3 equilibrium phase diagram [24].

Table 3 shows the electrical parameters derived from the Arrhenius plots of total conductivity. The conductivity in the low temperature region, characterised by that at 300°C (σ_{300}), and that in the high temperature region, characterised by that at 800°C (σ_{800}), both show decreasing trends with increasing Yb content. The σ_{800} values are high, especially in Y-rich compositions.

There is little compositional variation in the low temperature activation energy, ΔE_{LT}, in yttrium containing compositions, with only the fully Yb substituted composition showing a small decrease in activation energy. In contrast, the activation energy in the high temperature region, ΔE_{HT}, shows a maximum at x = 0.50 (Fig. 9). Another characteristic parameter is the pre-exponential factor, σ_0 in the Arrhenius expression for conductivity. This parameter is related to configurational entropy (ΔS):

$$\sigma_0 \propto \exp\left(-\frac{\Delta S}{k}\right) \qquad (2)$$

where k is the Boltzmann constant. In double substituted systems, such as in the present case, the values for configurational entropy are higher than in single substituted analogues. Fig. 9 shows that a maximum in σ_0 is obtained at high temperatures for the composition containing equal amounts of Y and Yb. These maxima in activation energy and pre-exponential factor are somewhat reminiscent of the well-known “mixed alkali effect” that occurs particularly in glasses [37], where a minimum in electrical conductivity and a maximum in activation energy are observed in ternary glass systems containing two dissimilar modifying oxides [38,39], at a fixed total cation content. The effect is not unknown in crystalline solids [40]. In most cases the mixing effect is associated with the more mobile sublattice and is also known as the “mixed mobile ion effect” [41]. However, in the present case it is associated with the immobile sublattice, rather than the mobile sublattice and there is no corresponding minimum in conductivity.

Fig. 10 shows the ionic and electronic contributions to total conductivity for the x = 0.00, 0.50 and 1.00 compositions. In all cases the total conductivity is found to be constituted almost entirely of the ionic component. Interestingly, for the x = 1.00 composition a large

drop in total conductivity is observed at around 600°C, which is associated with a change in ionic conductivity, rather than with any significant change in electronic conductivity. This temperature corresponds to the region of thermal hysteresis shown in Fig. 8 and the difference in the plots of total conductivity for the x = 1.00 composition between Figs. 7 and 10 results from the different time scales of the two experiments; the transference number experiments were taken over a much longer time period, allowing for a greater degree of phase separation.

Fig. 11 shows the thermal variation of ionic transference number for the x = 0.00, 0.50 and 1.00 compositions. The plots show that at temperatures above *ca*. 600°C all samples possess oxide ion transference numbers close to unity. Below 600°C, the x = 1.00 composition shows a significant decrease in oxide ion transference number to a value of around 89% at *ca*. 470°C. This correlates with the decrease in ionic conductivity seen in Fig. 10 below 600°C. The decrease in ionic transference number at lower temperatures is also reflected, but to a much lesser extent, in the plots for the x = 0.00 and x = 0.50 compositions, with the ionic contribution to total conductivity at low temperatures decreasing with increasing Yb content.

4. Conclusions

A full solid solution is observed in the pseudo-binary system Bi_3YO_6-Bi_3YbO_6, which exhibits a fully disordered δ-Bi_2O_3 type structure. Substitution of Y^{3+} by Yb^{3+} is found to favour a more centralised distribution of oxide ions in the tetrahedral cavity. Maxima in the high temperature activation energy and the pre-exponential factor are seen at the composition with equal amounts of Yb and Y. This can be associated with a maximum in configurational entropy. This effect may be analogous to the “mixed alkali effect” in glasses, but in this case is associated with the immobile sublattice.

Compositions in the $Bi_3Y_{1-x}Yb_xO_6$ system show high conductivities at elevated temperatures, with oxide ion transference numbers close to unity above *ca*. 600°C. There is evidence for conductivity decay in Yb rich compositions, which is probably associated with phase separation over long timescales.

Acknowledgements

We thank the Science and Technologies Facilities Council (STFC) ISIS Facility for neutron beam time and Dr Ron Smith for his help in data collection. We gratefully acknowledge the

National Science Centre Poland for project grant number 2012/05/E/ST3/02767 and the National Centre for Research and Development Poland for project grant number DKO/PL-TW1/6/2013.

References

1. E.D. Wachsman, K.T. Lee, Science 334 (2011) 935.

2. E.D. Wachsman, C. A. Marlowe, K.T. Lee, Energy Env. Sci. 5 (2012) 5498.

3. T. Takahashi, H. Iwahara, Y. Nagaj, J. Appl. Electrochem. 2 (1972) 97.

4. G. Mairesse, in Fast Ion Transport in Solids, B. Scrosati, A. Magistris, C.M. Mari, G. Mariotto (Eds.), Kluwer Academic Publishers, Dordrecht, 1993, p271.

5. J.C. Boivin, G. Mairesse, Chem. Mater. 10 (1998) 2870.

6. P. Shuk, H.D. Wiemhöfer, U. Guth, W. Göpel, M. Greenblatt, Solid State Ionics 89 (1996) 179.

7. N.M. Sammes, G.A. Tompsett, H. Näfe, F. Aldinger, J. Eur. Ceram. Soc. 19 (1999) 1801.

8. A.M. Azad, S. Larose, S.A. Akbar, J. Mater. Sci. 29 (1994) 4135.

9. M. Drache, P. Rooussel, J-P. Wignacourt, Chem. Rev. 107 (2007) 80.

10. A. Watanabe, Solid State Ionics 40/41 (1990) 889.

11. A. Watanabe, Solid State Ionics 86-88 (1996) 1427.

12. A. Watanabe, M. Sekita, Solid State Ionics 176 (2005) 2429.

13. K.Z. Fung H.D. Baek, A. Virkar, Solid State Ionics 52 (1992) 199.

14. K. Huang, M. Feng, J. B. Goodenough, Solid State Ionics 89 (1996) 17.

15. N. Jiang, E.D. Wachsman, S.-H. Jung, Solid State Ionics 150 (2002) 347.

16. S. K. Hahn and D. A. Stevenson, J. Chem. Thermodyn. 11 (1979) 627.

17. G. Meng, C. Chen, X. Han, P. Yang, D. Peng, Solid State Ionics 28-30 (1988) 533.

18. T. Takahashi, H. Iwahara, T. Arao, J. Appl. Electrochem. 5 (1975) 187.

19. R. Punn, A.M. Feteira, D.C. Sinclair, C. Greaves, J. Am. Chem. Soc. 128 (2006) 128 15386.

20. R.K. Datta, J.P. Meehan, Z. Anorg. Allgem. Chem. 383 (1971) 328.

21. A. Watanabe, T. Kikuchi, Solid State Ionics 21 (1986) 287.

22. H. Iwahara, T. Esaka, T. Sato, T. Takahashi, J. Solid State Chem. 39 (1981) 173.

23. X.L. Chen, F.F. Zhang, Y.M. Shen, J.K. Liang, W.H. Tang, Q.Y. Tu, J Solid State Chem. 139 (1998) 398.

24. M. Drache, P. Roussel, J.P. Wignacourt, P. Conflant, Mater. Res. Bull. 39 (2004) 1393.

25. S. Boyapati, E.D. Wachsman, B.C. Chakoumakos, Solid State Ionics 138 (2001) 293.

26. S. Boyapati, E.D. Wachsman, N. Jiang, Solid State Ionics 140 (2001) 149.

27. E.D. Wachsman, J. Eur. Ceram. Soc. 24 (2004) 1281.

28. P.D. Battle, C.R.A. Catlow, J. Drennan, A.D. Murray, J. Phys. C 16 (1983) 561.

29. I. Abrahams, X. Liu, S. Hull, S.T. Norberg, F. Krok, A. Kozanecka-Szmigiel, M. S. Islam, S.J. Stokes, Chem. Mater. 22 (2010) 4435.

30. R.D. Shannon, Acta Crystallogr. A32 (1976) 751.

31. J.R. Dygas, P. Kurek, M.W. Breiter, Electrochim. Acta 40 (1995) 1545.

32. M. Malys, J.R. Dygas, M. Holdynski, A. Borowska-Centkowska, W. Wrobel, M. Marzantowicz, Solid State Ionics 225 (2012) 493.

33. A. C. Larson, R. B. Von Dreele, Los Alamos National Laboratory Report, No. LAUR-86-748, (1987).

34. I. Abrahams, A. Kozanecka-Szmigiel, F. Krok, W. Wrobel, S.C.M. Chan, J.R. Dygas, Solid State Ionics 177 (2006) 1761.

35. M. Leszczynska, X. Liu, W. Wrobel, M. Malys, S.T. Norberg, S. Hull, F. Krok, I. Abrahams, J. Phys.: Condens. Matter. 25 (2013) 454207.

36. M. Leszczynska, X. Liu, W. Wrobel, M. Malys, M. Krynski, S.T. Norberg, S. Hull, F. Krok, I. Abrahams, Chem. Mater. 25 (2013) 326.

[37] J.O. Isard. J. Non-Cryst. Solids 1 (1969) 235.

[38] J.C. Lapp, J.E. Shelby, J. Non-Cryst. Solids 86 (1986) 350.

[39] C.-P.E. Varsamis, E.I. Kamitos, G.D. Chryssikos, Phys. Chem. Glasses 41 (2000) 242.

[40] M. Meyer, V. Jaenisch, P. Maass, and A.Bunde, Phys. Rev. Lett. 76 (1996) 2338.

[41] V. Belostotsky, J. Non-Cryst. Solids 353 (2007) 1078.

Table 1. Crystal and refinement parameters for $Bi_3Y_{1-x}Yb_xO_6$ at room temperature.[a]

Composition	x = 0.25	x = 0.50	x = 0.75
Chemical formula	$Bi_3Yb_{0.75}Yb_{0.25}O_6$	$Bi_3Yb_{0.5}Yb_{0.5}O_6$	$Bi_3Yb_{0.25}Yb_{0.75}O_6$
Formula weight	832.873	853.908	874.940
Crystal system	Cubic	Cubic	Cubic
Space group	*Fm*-3*m*	*Fm*-3*m*	*Fm*-3*m*
Unit cell dimension	a = 5.48207(3) Å	a = 5.47634(8) Å	a = 5.47060(9) Å
Volume	164.753(3) $Å^3$	164.237(7) $Å^3$	163.722(9) $Å^3$
Z	1	1	1
Density (calculated)	8.395 Mg m^{-3}	8.634 Mg m^{-3}	8.874 Mg m^{-3}
μ (CuKα X-ray)	169.40 mm^{-1}	173.40 mm^{-1}	177.43 mm^{-1}
F(000)	343.75	351.50	359.25
Sample description	Yellow powder	Yellow powder	Yellow powder
R-factors[a]	Neutron (back-scattering) R_{wp} = 0.0278, R_p = 0.0401 R_{ex} = 0.0097, R_F2 = 0.0576 Neutron (low angle) R_{wp} = 0.0245, R_p = 0.0197, R_{ex} = 0.0271, R_F2 = 0.0547 X-ray R_{wp} = 0.0437, R_p = 0.0290, R_{ex} = 0.0231, R_F2 = 0.0752 Totals R_{wp} = 0.0316, R_p = 0.0289 χ^2 = 4.004	Neutron (back-scattering) R_{wp} = 0.0129, R_p = 0.0186 R_{ex} = 0.0083, R_F2 = 0.0564 Neutron (low angle) R_{wp} = 0.0213, R_p = 0.0170, R_{ex} = 0.0229, R_F2 = 0.0614 X-ray R_{wp} = 0.0645, R_p = 0.0500, R_{ex} = 0.0507, R_F2 = 0.1229 Totals R_{wp} = 0.0171, R_p = 0.0463 χ^2 = 1.628	Neutron (back-scattering) R_{wp} = 0.0158, R_p = 0.0239 R_{ex} = 0.0073, R_F2 = 0.0706 Neutron (low angle) R_{wp} = 0.0206, R_p = 0.0165, R_{ex} = 0.0200, R_F2 = 0.0571 X-ray R_{wp} = 0.0651, R_p = 0.0510, R_{ex} = 0.0533, R_F2 = 0.0796 Totals R_{wp} = 0.0183, R_p = 0.0467 χ^2 = 2.408
No. of variables	124	124	124
No of profile points used	3247 (Neutron,back-scattering) 3521 (Neutron,low-angle) 6282 (X-ray)	3248 (Neutron,back-scattering) 3572 (Neutron,low-angle) 3141 (X-ray)	3248 (Neutron,back-scattering) 3521 (Neutron,low-angle) 3141 (X-ray)
No of reflections	41 (Neutron,back-scattering) 46 (Neutron,low-angle) 31 (X-ray)	39 (Neutron,back-scattering) 48 (Neutron,low-angle) 31 (X-ray)	38 (Neutron,back-scattering) 41 (Neutron,low-angle) 30 (X-ray)

[a]For definition of R-factors see [33].

Table 2. Refined structural parameters and significant contact distances (Å) for $Bi_3Y_{1-x}Yb_xO_6$ at room temperature.

Composition	x = 0.25	x = 0.50	x = 0.75
Chemical formula	$Bi_3Yb_{0.75}Yb_{0.25}O_6$	$Bi_3Yb_{0.5}Yb_{0.5}O_6$	$Bi_3Yb_{0.25}Yb_{0.75}O_6$
Bi/Y/Yb site	4*a*	4*a*	4*a*
Bi/Y/Yb Occ.	0.75/0.188/0.063	0.75/0.125/0.125	0.75/0.063/0.188
Bi/Y/Yb U_{iso} (Å^2)	0.0482(4)	0.0459(3)	0.0475(3)
O(1) site	8*c*	8*c*	8*c*
O(1) Occ.	0.396(9)	0.371(6)	0.355(7)
O(1) U_{iso} (Å^2)	0.0655(10)	0.0644(6)	0.0654(6)
O(2) site	32*f*	32*f*	32*f*
O(2) *x*, *y*, *z*	0.3101(12)	0.3069(7)	0.3067(7)
O(2) Occ.	0.071(2)	0.078(2)	0.081(2)
O(2) U_{iso} (Å^2)	0.0655(10)	0.0644(6)	0.0654(6)
O(3) site	48*i*	48*i*	48*i*
O(3) *y*, *z*	0.2024(25)	0.1997(15)	0.1980(16)
O(3) Occ.	0.012(1)	0.011(1)	0.012(1)
O(3) U_{iso} (Å^2)	0.0655(10)	0.0644(6)	0.0654(6)
Bi/Y/Yb-O(1)	2.37381(1)	2.37133(3)	2.36884(3)
Bi/Y/Yb-O(2)	2.2489(12)	2.2497(7)	2.2475(8)
Bi/Y/Yb-O(3)	1.973(4)	1.9750(22)	1.9756(25)

Table 3. Electrical parameters for $Bi_3Y_{1-x}Yb_xO_6$: low temperature activation energy (ΔE_{LT}), high temperature activation energy (ΔE_{HT}), total conductivity at 300˚C (σ_{300}), total conductivity 800˚C (σ_{800}) and pre-exponential factor σ_0. Parameters correspond to the second cooling run.

x	**σ_{300} / S cm^{-1}**	**σ_{800} / S cm^{-1}**	**ΔE_{LT} / eV**	**ΔE_{HT} / eV**	**σ_0 at 300˚C**	**σ_0 at 800˚C**
0.00	$6.1(5) \times 10^{-5}$	0.77(3)	1.147(4)	0.679(3)	4.29×10^{8}	1.27×10^{6}
0.25	$4.3(1) \times 10^{-5}$	0.57(4)	1.140(2)	0.676(6)	2.64×10^{8}	9.13×10^{5}
0.50	$4.1(2) \times 10^{-5}$	0.55(5)	1.148(2)	0.690(9)	2.90×10^{8}	1.03×10^{6}
0.75	$2.2(6) \times 10^{-5}$	0.38(4)	1.140(1)	0.674(9)	1.37×10^{8}	6.01×10^{5}
1.00	$1.9(3) \times 10^{-5}$	0.21(15)	1.009(9)	0.59(7)	7.98×10^{6}	1.37×10^{5}

Figure Captions

Fig.1. Fitted diffraction profiles for $Bi_3Y_{1-x}Yb_xO_6$ at room temperature for x = 0.25 (a) to (c), x = 0.50 (d) to (f) and x = 0.75 (g) to (i). Neutron back scattering (a), (d) and (g), neutron low angle (b), (e) and (h) and X-ray (c), (f) and (i) data are shown. Observed (+ symbols), calculated (line) and difference (lower) profiles are shown, with reflection positions indicated by markers.

Fig. 2. Compositional variation of cubic lattice parameter in $Bi_3Y_{1-x}Yb_xO_6$ at room temperature and 800°C. Results for x = 0.00 and x = 1.00 are taken from previous studies [29,35].

Fig. 3. Variable temperature X-ray powder diffraction patterns for $Bi_3Y_{0.5}Yb_{0.5}O_6$ on heating and cooling.

Fig. 4. Thermal variation of cubic lattice parameter in $Bi_3Y_{1-x}Yb_xO_6$.

Fig. 5. DTA thermogram for $Bi_3Y_{0.5}Yb_{0.5}O_6$. Heating and cooling directions are indicated by arrows.

Fig. 6. Compositional variation of oxide ion site occupancies in $Bi_3Y_{1-x}Yb_xO_6$ at room temperature, derived from combined X-ray and neutron refinements. Plotted values are fraction of total oxide content. Estimated standard deviations are indicated.

Fig. 7. Arrhenius plots of total conductivity for compositions in the system $Bi_3Y_{1-x}Yb_xO_6$. Data correspond to second cooling run.

Fig. 8. Arrhenius plots of total conductivity for Bi_3YbO_6 (x = 1.00) from two successive heating and cooling cycles.

Fig. 9. Compositional variation of high temperature activation energy ΔE_{HT} and total conductivity pre-exponential factor, σ_0.

Fig. 10. Arrhenius plots of conductivity for $Bi_3Y_{1-x}Yb_xO_6$ (a) x = 0.00, (b) x = 0.50 and (c) x = 1.00, showing total, ionic and electronic conductivities on cooling.

Fig. 11. Thermal variation of ionic transference number in $Bi_3Y_{1-x}Yb_xO_6$.

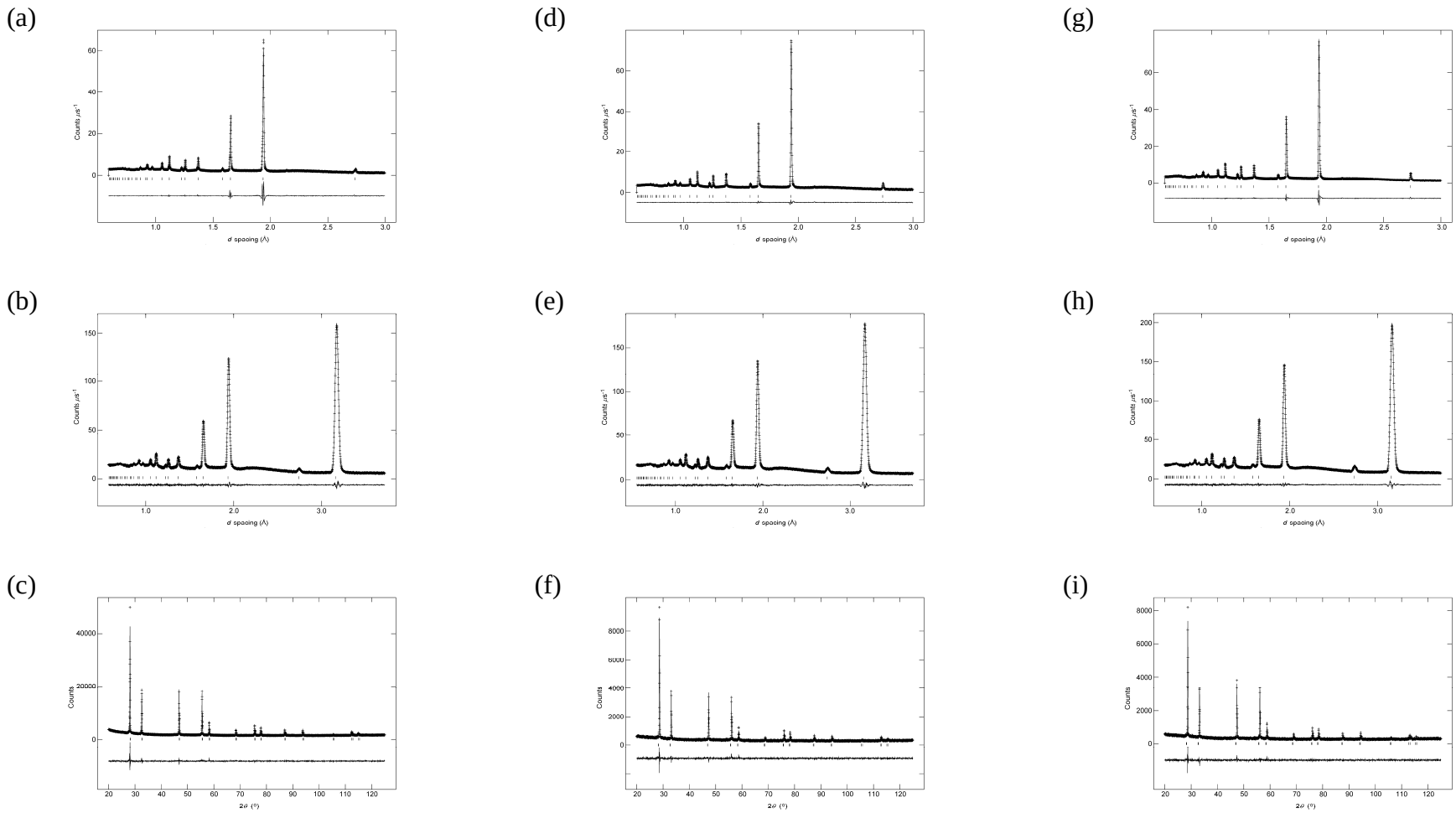

Fig.1. Fitted diffraction profiles for $Bi_3Y_{1-x}Yb_xO_6$ at room temperature for x = 0.25 (a) to (c), x = 0.50 (d) to (f) and x = 0.75 (g) to (i). Neutron back scattering (a), (d) and (g), neutron low angle (b), (e) and (h) and X-ray (c), (f) and (i) data are shown. Observed (+ symbols), calculated (line) and difference (lower) profiles are shown, with reflection positions indicated by markers.

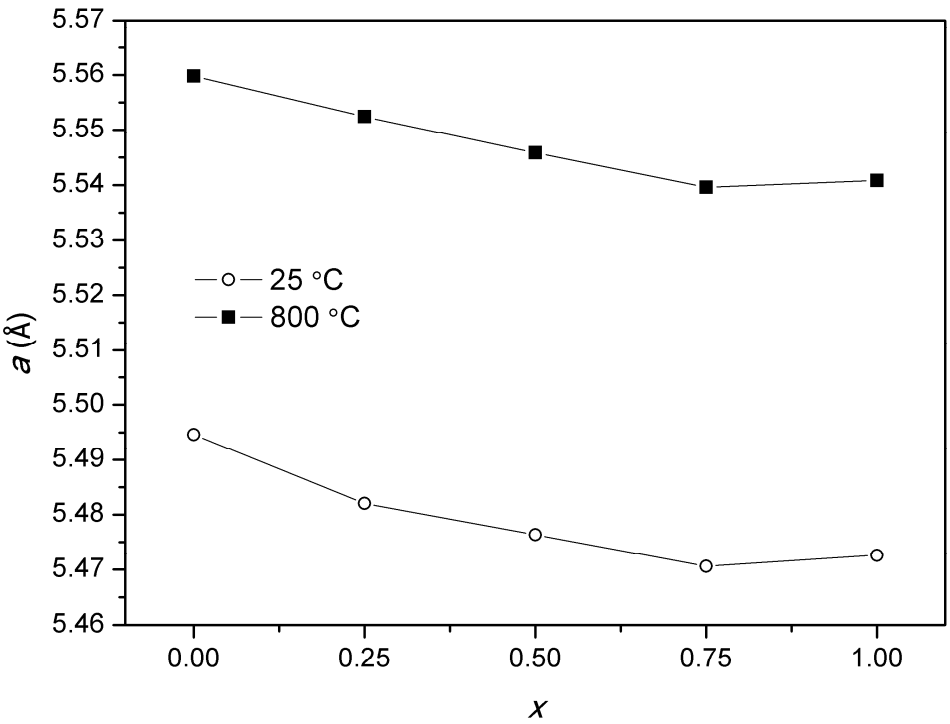

Fig. 2. Compositional variation of cubic lattice parameter in $Bi_3Y_{1-x}Yb_xO_6$ at room temperature and 800°C. Results for x = 0.00 and x = 1.00 are taken from previous studies [29,35].

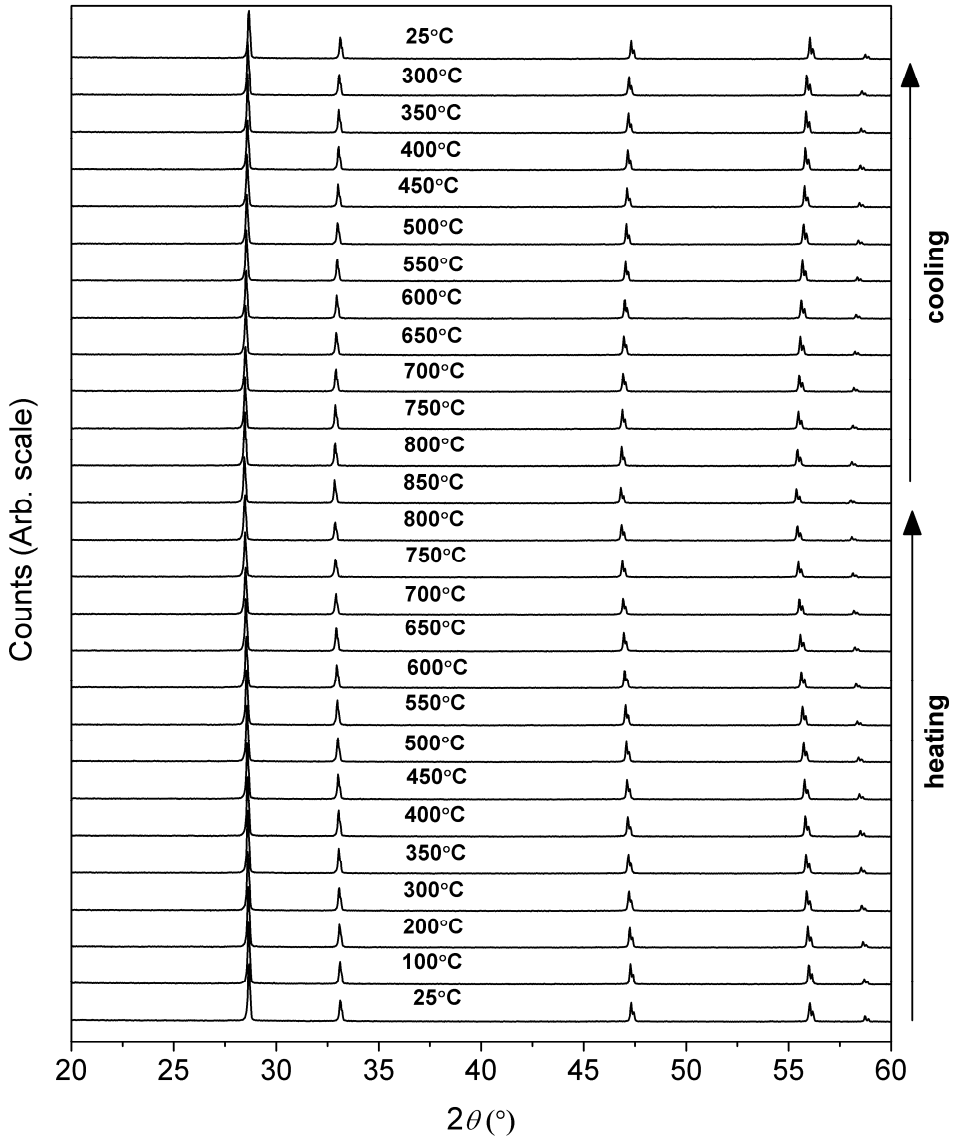

Fig. 3. Variable temperature X-ray powder diffraction patterns for $Bi_3Y_{0.5}Yb_{0.5}O_6$ on heating and cooling.

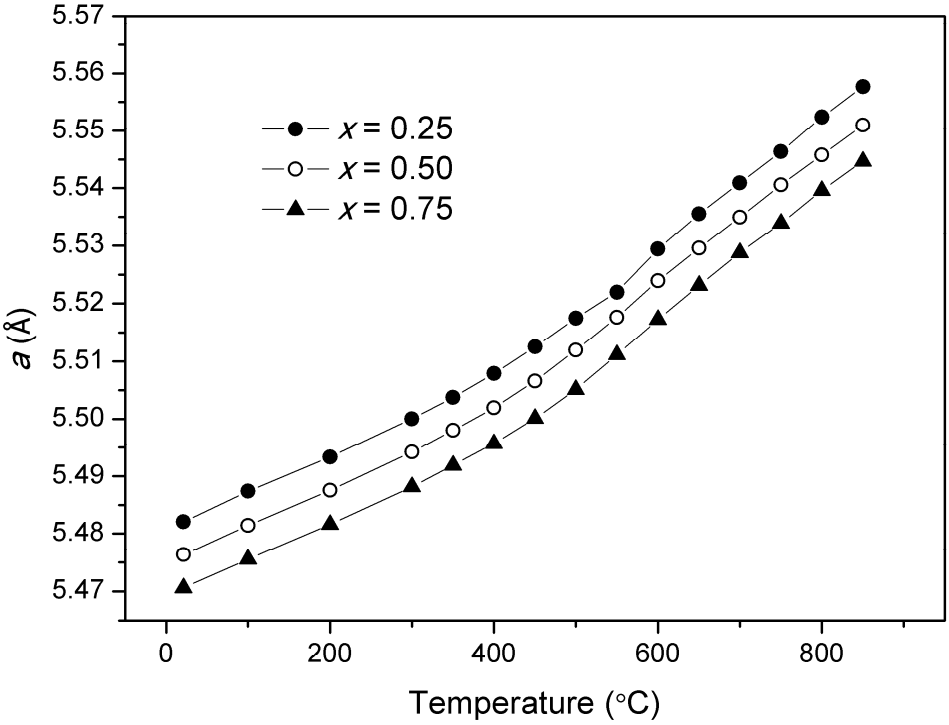

Fig. 4. Thermal variation of cubic lattice parameter in $Bi_3Y_{1-x}Yb_xO_6$

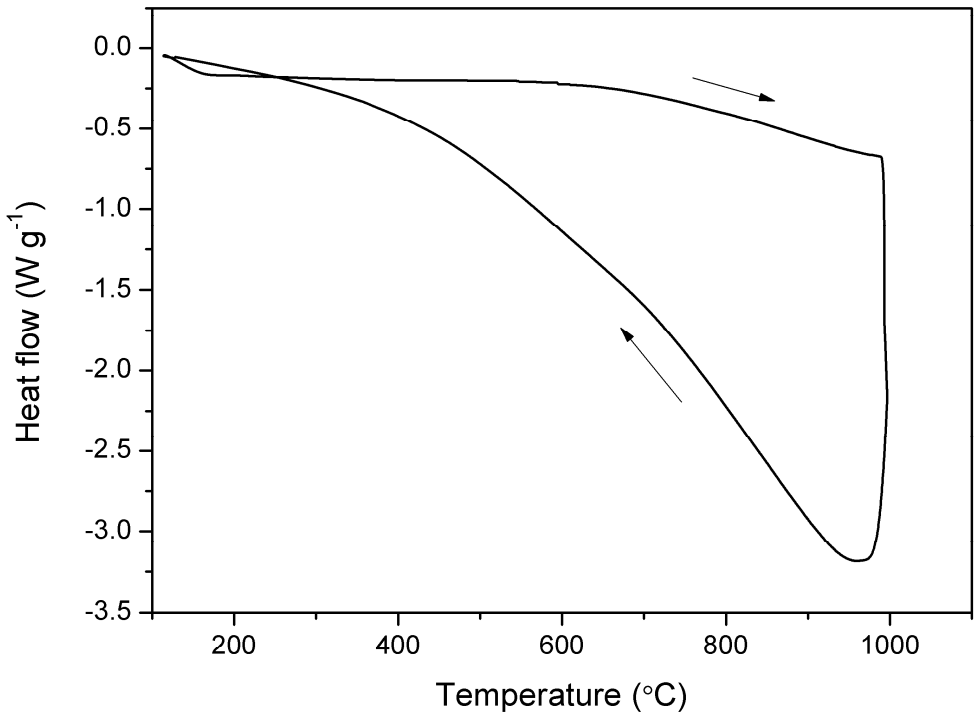

Fig. 5. DTA thermogram for $Bi_3Y_{0.5}Yb_{0.5}O_6$. Heating and cooling directions are indicated by arrows.

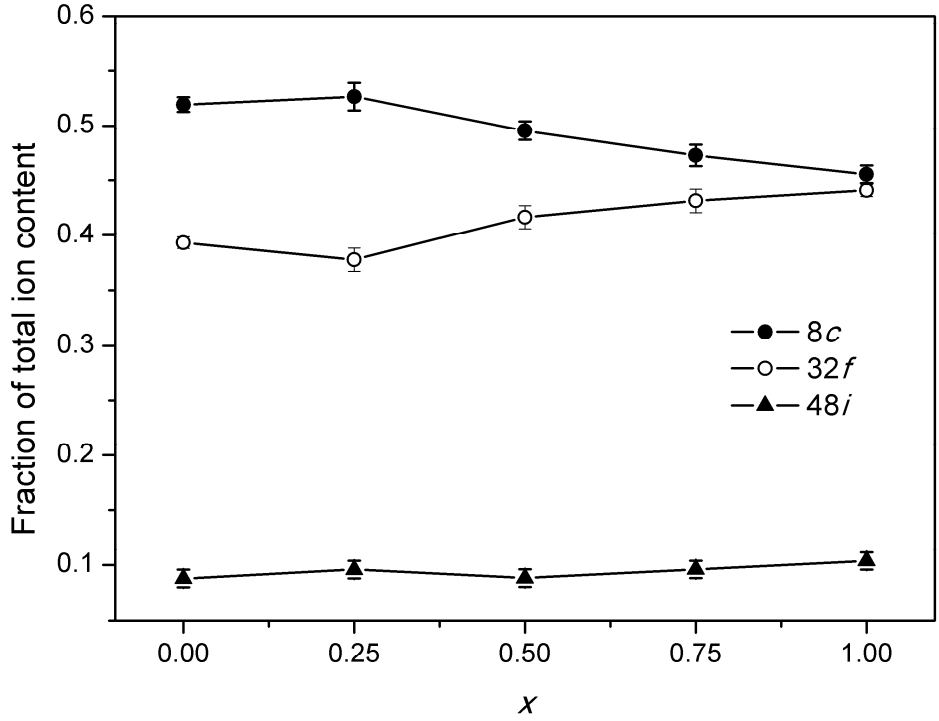

Fig. 6. Compositional variation of oxide ion site occupancies in $Bi_3Y_{1-x}Yb_xO_6$ at room temperature, derived from combined X-ray and neutron refinements. Plotted values are fraction of total oxide content. Estimated standard deviations are indicated.

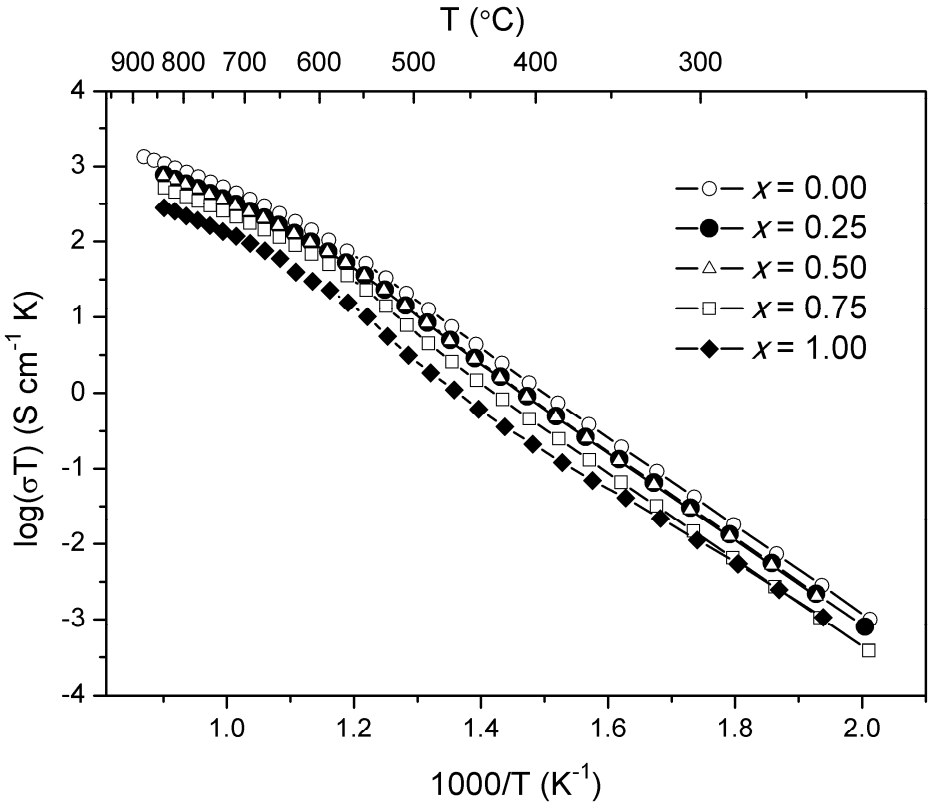

Fig. 7. Arrhenius plots of total conductivity for compositions in the system $Bi_3Y_{1-x}Yb_xO_6$. Data correspond to second cooling run.

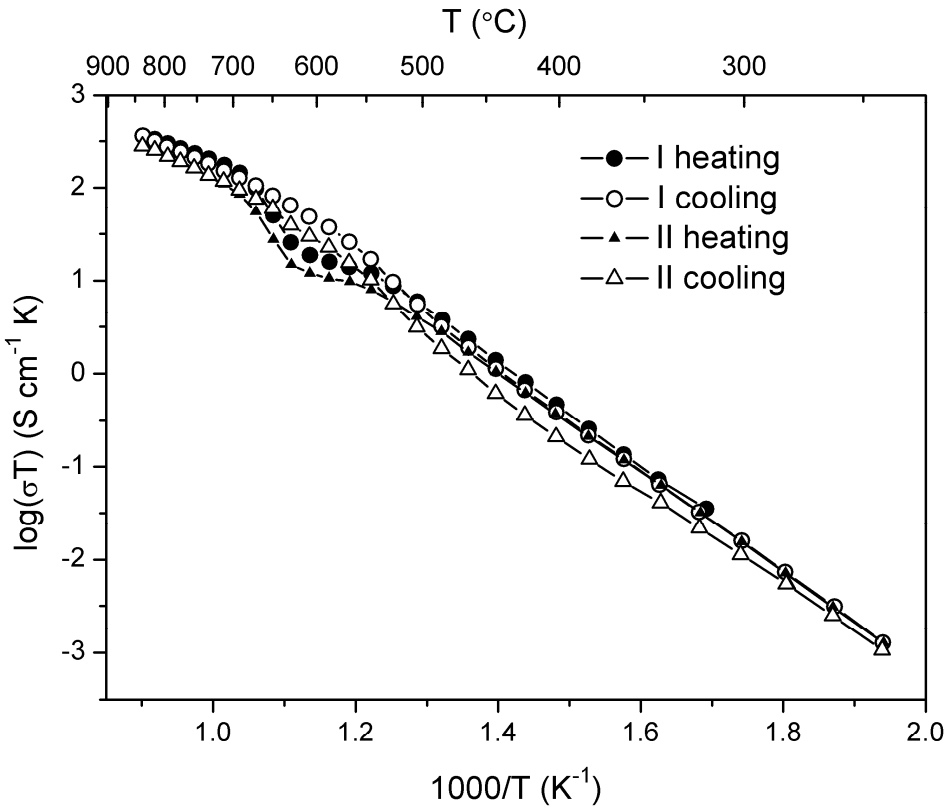

Fig. 8. Arrhenius plots of total conductivity for Bi_3YbO_6 (x = 1.00) from two successive heating and cooling cycles.

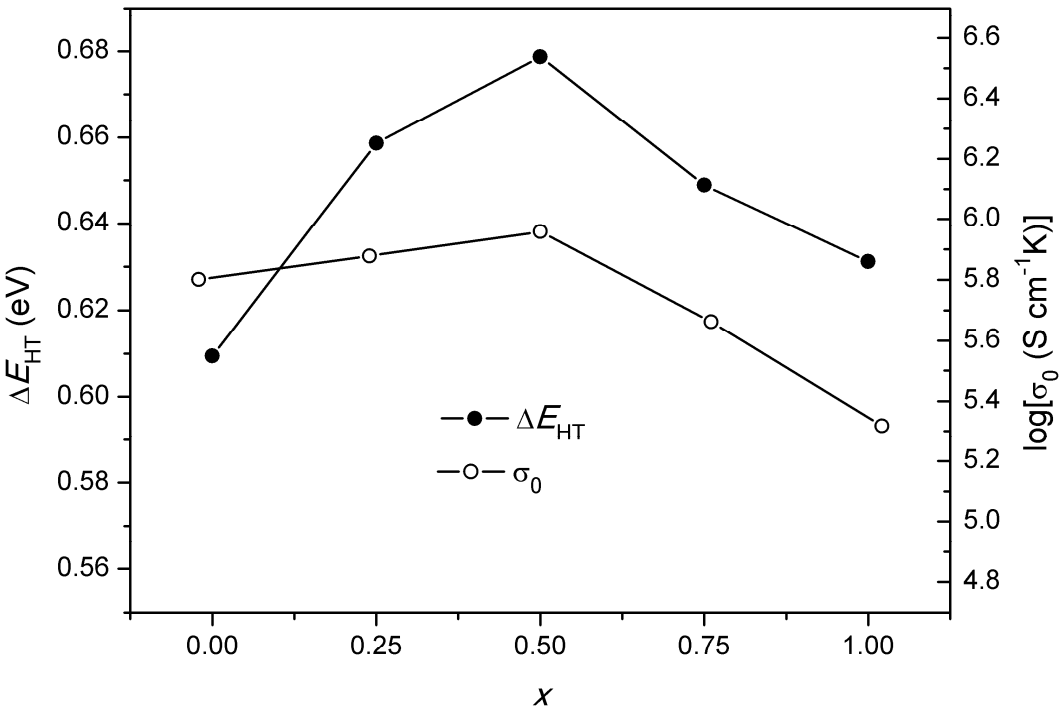

Fig. 9. Compositional variation of high temperature activation energy ΔE_{HT} and total conductivity pre-exponential factor, σ_0.

(a)

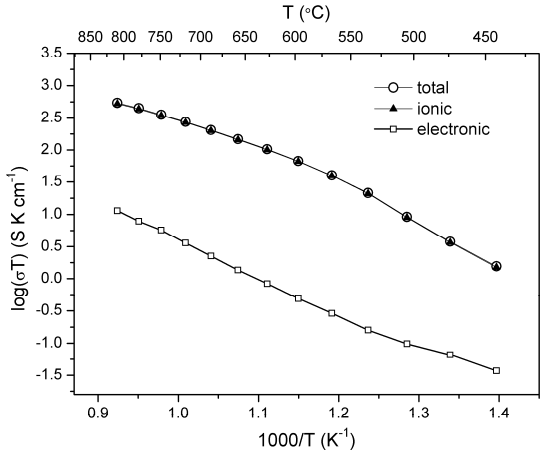

(b)

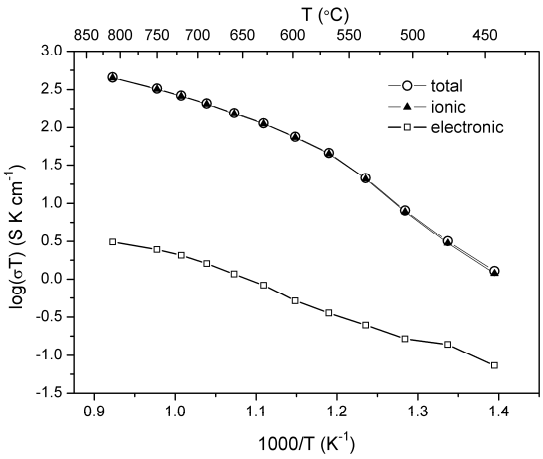

(c)

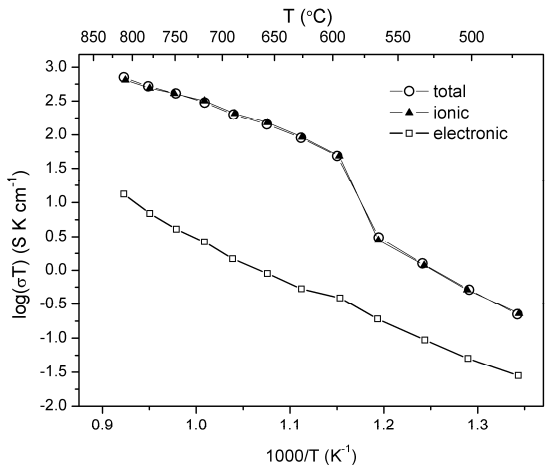

Fig. 10. Arrhenius plots of conductivity for $Bi_3Y_{1-x}Yb_xO_6$ (a) x = 0.00, (b) x = 0.50 and (c) x = 1.00, showing total, ionic and electronic conductivities on cooling.

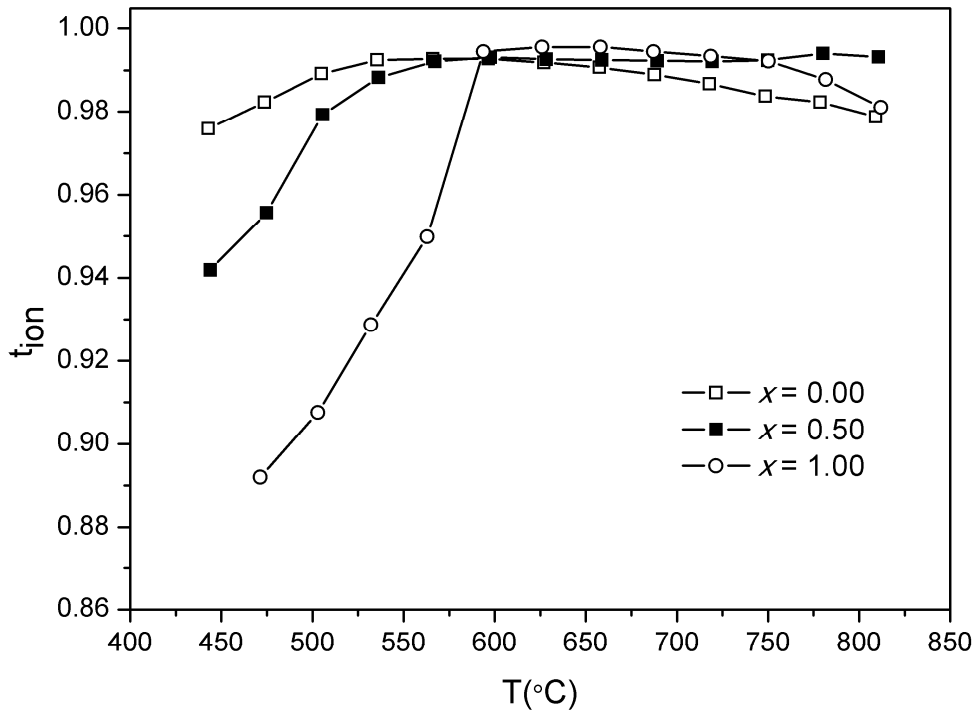

Fig. 11. Thermal variation of ionic transference number in $Bi_3Y_{1-x}Yb_xO_6$.